Influence of pH on the Human Prion Protein: Insights into the Early Steps of Misfolding

Marc W. van der Kamp and Valerie Daggett*
Department of Bioengineering, University of Washington, Seattle, Washington

ABSTRACT Transmissible spongiform encephalopathies, or prion diseases, are caused by misfolding and aggregation of the prion protein PrP. Conversion from the normal cellular form (PrP^C) or recombinant PrP (recPrP) to a misfolded form is pH-sensitive, in that misfolding and aggregation occur more readily at lower pH. To gain more insight into the influence of pH on the dynamics of PrP and its potential to misfold, we performed extensive molecular-dynamics simulations of the recombinant PrP protein (residues 90–230) in water at three different pH regimes: neutral (or cytoplasmic) pH (~7.4), middle (or endosomal) pH (~5), and low pH (<4). We present five different simulations of 50 ns each for each pH regime, amounting to a total of 750 ns of simulation time. A detailed analysis and comparison with experiment validate the simulations and lead to new insights into the mechanism of pH-induced misfolding. The mobility of the globular domain increases with decreasing pH, through displacement of the first helix and instability of the hydrophobic core. At middle pH, conversion to a misfolded (PrP^{Sc}-like) conformation is observed. The observed changes in conformation and stability are consistent with experimental data and thus provide a molecular basis for the initial steps in the misfolding process.

INTRODUCTION

Transmissible spongiform encephalopathies (TSEs), or prion diseases, are fatal neurodegenerative disorders that occur in a range of mammals. These disorders include Creutzfeldt-Jakob disease (CJD) and kuru in humans, scrapie in sheep, bovine spongiform encephalopathy in cattle, and chronic wasting disease in cervids. In humans, TSEs can arise spontaneously, via inheritance of predisposing mutations, or by infection (1,2). The disorders are characterized by aggregates of the prion protein PrP that accumulate in neuronal cells, although it is not yet clear what type of PrP particle is neurotoxic (3,4). Misfolding and aggregation of the normal cellular form of the prion protein (PrP^C) to a largely proteinase K resistant aggregate (PrP^{Sc}) is the central event in the development of TSE diseases. Propagation of PrP^{Sc}, which is relevant for spreading of disease within individuals as well as through cross-species infection, is believed to occur through recruitment of PrP^C by the PrP^{Sc} template. An understanding of the location, circumstances, and mechanism of both the initial PrP^C misfolding and the subsequent propagation is of great importance for the detection, treatment and prevention of TSE diseases.

Mature human PrP contains 208 residues (residues 23–230; human numbering is used throughout), is attached to a membrane with a glycosylphosphatidyl-inositol (GPI) anchor, and can be glycosylated in two positions. The N-terminal region (residues 23–127) is highly flexible (5–8), and the C-terminal part (residues 128–228) is folded and contains three α-helices (HA, HB, and HC) and a short, two-stranded antiparallel β-sheet (S1 and S2; Fig. 1 *A*). Apart from an increase in β-sheet content (9–11), details about how the PrP structure changes upon misfolding and aggregation are not known. This is largely due to the difficulty of obtaining detailed structural information for protein aggregates, and the experimental challenges posed by working with brain-derived PrP. Many studies have therefore been performed using recombinant PrP (recPrP), which usually consists of residues 90–230/231 and lacks the GPI-anchor and glycosylation. This fragment is relevant for studying conversion of PrP^C to PrP^{Sc}, as purification of PrP^{Sc} aggregates most commonly results in PrP subunits of residues ~90–230. The fragment includes regions that are crucial for aggregation (residues 98–110 and 136–140) (12), the neurotoxic peptide 106–126 (13,14), and the toxic and infectious construct PrP^{Sc}106 (15).

About 85% of cases of fatal prion disease in humans are sporadic forms of CJD for which no association with mutations or exposure to TSE-infected material is evident. It is therefore likely that PrP^C can misfold spontaneously, but such misfolding must be a rare event in vivo. PrP^C molecules located on the outer cellular membrane are regularly taken into the cell through the endosomal pathway (16). The pH environment in endosomes is relatively low (pH ~5) (17), and it has been suggested that misfolding of PrP in sporadic TSE disease occurs there (18–21). Various in vitro studies have reported a relationship between low pH and misfolding and aggregation of PrP (22). In particular, significant conformational changes in human recPrP occur between pH 6 and 4.4 (23), and spontaneous fibril formation of human recPrP occur under conditions of pH 4.0 and slow rotation (24). Furthermore, the thermodynamic stability of PrP decreases significantly when the pH is lowered from pH 7 to pH 4.8 (25) or pH 4.5 (26).

Submitted June 30, 2010, and accepted for publication July 27, 2010.

*Correspondence: daggett@u.washington.edu

Editor: Ruth Nussinov.

0006-3495/10/10/2289/10 $2.00

doi: 10.1016/j.bpj.2010.07.063

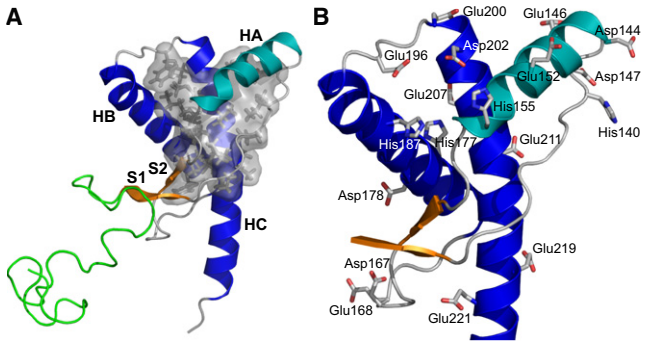

FIGURE 1 Structure of human PrP 90–230. (*A*) Starting structure of recombinant PrP used for the simulations, based on the NMR solution structure obtained at pH 4.5 (7). Secondary structure elements are labeled and the side chains and surface of the residues in the hydrophobic core (51) are shown. (*B*) The same structure as in panel *A* (but truncated), with all His, Asp, and Glu residues in the globular domain shown and labeled. (The flexible N-terminus contains His^{96} and His^{111} and no Asp or Glu residues.)

Despite the destabilizing effects of low pH, a previous NMR study (26) indicated that there is little difference between the global conformation of PrP at pH 7 and pH 4.5. It is possible, however, that misfolded conformations were not detected in that study due to a relatively small fraction and/or structural diversity of misfolded conformations and aggregation. Previous molecular-dynamics (MD) studies by our group indicate that low pH can promote conversion of PrP to a misfolded form (27–30), which includes extension of the native β-sheet. This misfolded form can be fit into a spiral protofibril, which may represent the early aggregation phase of PrP (PrP^{Sc}) and the infectious or neurotoxic particle (29,31).

Here, we expand upon previous studies and perform extensive explicit-solvent MD simulations of wild-type recPrP using three different setups representing three different pH ranges. The simulations are significantly longer (50 ns each) than those used in the vast majority of published MD studies on PrP, and five separate simulations were performed for each of the pH ranges to obtain more comprehensive conformational sampling than is possible through single MD trajectories. The total simulation time amounts to 750 ns, or 0.75 μs. We analyze the differences between neutral- and lower-pH regimes in detail and on a large scale, which allows for the identification of general structural and dynamical changes to human PrP caused by a shift to lower pH. Furthermore, conformational changes consistent with conversion are observed in one of the simulations in the mildly acidic pH range, which is representative of the pH used for in vitro conversion of recPrP (24) and the pH of endocytic compartments (17). The mechanism of this conformational change is described in detail.

METHODS

The starting structure for all simulations was based on human PrP at pH 4.5, Protein Data Bank (PDB) code 1QLX (7). The missing flexible N-terminal residues were modeled in accordance with nuclear Overhauser effect (NOE) data and placed such that they were free to move in different directions without biasing the simulations (Fig. 1). The resulting PrP structure (residues 90–230) was further prepared in three different ways to reflect three different pH ranges: neutral (histidines neutral and other titratable side chains charged, pH ~7–8), middle (all titratable side chains charged, pH ~5, i.e., His protonated), and low (all titratable side chains protonated, i.e., Glu and Asp protonated in addition to His, pH 3–4). At neutral pH, His^{144} was protonated on Nδ1 and all other histidines were protonated on Nε2.

Explicit solvent all-atom MD simulations were performed at 298 K with *in lucem* molecular mechanics (*il*mm) (32), employing the Levitt et al. (33) force field and the F3C water model (34) and using previously described protocols (35). Five simulations of 50 ns were performed at each pH range with different starting velocities. The total simulation time therefore amounted to 750 ns. Structures were saved every 1 ps. Cα root mean-square deviation (RMSD), Cα root mean-square fluctuation (RMSF), solvent-accessible surface area (SASA) (36), DSSP (Define Secondary Structure of Proteins) (37), and contact and NOE crosspeak analyses were performed with *il*mm (32). NOE data obtained for human E200K PrP (BMRB entry 4641) (38) were used. Atom-atom contacts were classified as follows: salt bridge (carboxyl oxygen (s) in contact with nitrogens of charged groups), hydrogen bond (donor-hydrogen-acceptor angle $> 135°$ and hydrogen-acceptor distance ≤ 2.6 Å), and hydrophobic (C−C distance between CH_n groups ≤ 5.4 Å). A detailed description of the methods used is available in the Supporting Material.

RESULTS AND DISCUSSION

Validation of simulation by comparison with NOE restraints

To assess the overall agreement of the MD simulations with experiment, we compared the results with the publicly available NOE restraints for human PrP with the E200K mutation, which is structurally very similar to WT PrP (38). We first determined the expected level of agreement by comparing the E200K restraints with the WT NMR structures for human PrP obtained at pH 4.5 and 7.0. The NMR bundles (PDB codes 1QLZ and 1HJN) showed a NOE restraint satisfaction of 90% for all NOEs and 79% for long-range NOEs. Consequently, this is the expected correspondence between WT and E200K. The structures sampled from our MD simulations showed similar satisfaction: 91%, 91%, and 90% of the total NOEs, and 76%, 77%, and 75% of the long-range NOEs for neutral, middle, and low pH, respectively. The overall simulation data are therefore in line with the experimental NMR data, indicating that our simulations sample experimentally relevant conformations. NOE restraint satisfaction was further measured for the individual trajectories as a function of simulation time (see Fig. S2). The neutral-pH simulations did not show a significant decline in satisfaction, whereas several middle- and low-pH simulations (three each) did. Such a decline signifies a drift in conformation away from the main structured ensemble, indicating that conformational changes may be occurring.

Cα RMSD as an indicator of structural stability

The Cα RMSD of the structured portion of the protein (the globular domain, residues 128–228) was used to monitor the stability and occurrence of conformational changes in that region (Fig. 2 *A*). The neutral-pH simulations showed

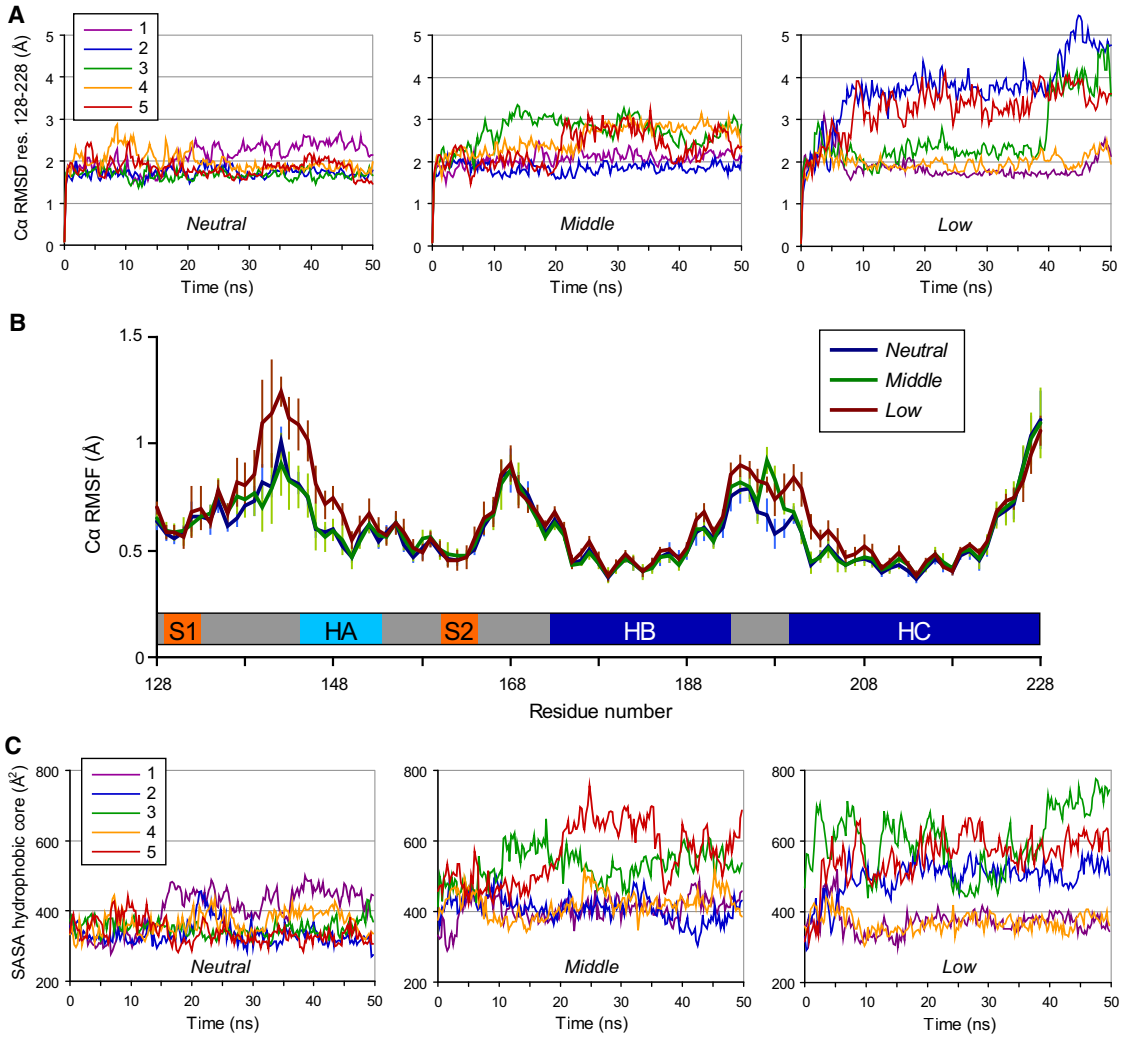

FIGURE 2 Stability and flexibility of PrP in the three different pH regimes. (*A*) Cα RMSD of the globular domain (residues 128–228). (*B*) Cα RMSF of the globular domain as calculated from 1 ns time windows throughout the trajectory and averaged over all five simulations for each pH regime. Vertical lines indicate the standard deviation across the five simulations, and secondary structure elements are indicated in the horizontal bar. (*C*) The SASA of the hydrophobic core, calculated as the side-chain SASA of the following residues: 134, 137, 139, 141, 158, 161, 175, 176, 179, 180, 184, 198, 203, 205, 206, 209, 210, and 213–215. For clarity, a windowed average over a period of 250 ps is shown in panels *A* and *C*.

only moderate changes in RMSD, whereas significant differences occurred in several middle- and low-pH simulations (particularly in middle-pH simulations 3, 4, and 5, and low-pH simulations 2, 3, and 5). The changes were most extreme in three low-pH simulations. Of interest, the RMSD of the other two low-pH simulations stayed low, in similarity to the neutral-pH simulations. This difference indicates a relatively rare but large conformational change happening in the low- and (to a lesser extent) middle-pH simulations. Visual inspection revealed large movements of HA in all simulations that reached Cα RMSD values > 3 Å, and a comparison of specific RMSD matrices confirmed that HA movement was the main contributor to the increase in Cα RMSD (Fig. S4). Cα RMSD was also measured for portions of HB and HC (linked by the disulfide bond) that form a stable helical core of the prion protein (7,8,26) (Fig. S3). Apart from one outlier (neutral-pH simulation 1), the Cα RMSD was ~1 Å in all simulations from 25 to 50 ns (see the Supporting Material). Experimental data indicate a conformational change and a decrease in stability with decreasing pH (23,25,26,40). Our simulations suggest that this instability is primarily related to increased movement outside the stable HB-HC core, in particular of HA.

Backbone flexibility probed by Cα RMSF

The RMSFs of the Cα atoms were measured from average structures calculated from 1 ns time windows throughout the trajectory. This procedure minimizes the influence of conformational changes on the magnitude of the fluctuations, providing an overall indication of backbone mobility. The flexibility of the N-terminal residues (residues 90–127) was

always high and on par with the flexibility of loops in the globular domain (Fig. S2). After residue 127 the Cα RMSF dropped sharply, marking the start of the structured globular domain. The Cα RMSF for this domain was calculated based on alignment of structures on residues 128–228 only, to avoid the influence of the unstructured N-terminal domain on the alignment and the subsequently calculated RMSF values (Fig. 2 *B*).

Generally, the secondary structure elements showed the lowest Cα RMSF values, and loops showed the highest. This trend was not observed in the C-terminal portions of HB and HC and the loop between HA and S2, in agreement with hydrogen/deuterium exchange protection factors (7,26). The loop also had a high backbone displacement in the NMR bundles (7,26). For the C-terminal portion of HC, there are many experimental indications of high flexibility: residues 220–231 are considered partly disordered in mouse PrP (41) and human PrP with the R220K mutation (42) and NMR relaxation studies on hamster and mouse PrP show fast picosecond timescale motions of the backbone amides from residue 222 (8,43). The NMR studies also indicated picosecond timescale motions in the loop between HB and HC, subnanosecond flexibility in the loop preceding HA (residues 137–141), and slow motions in residues flanking the unstructured loop between S2 and HB (8,43), which is in line with the increased Cα RMSF we observed for these loop regions.

The trend of flexibility was the same for simulations at the three pH regimes. Differences in Cα RMSF mostly existed in the loops between S1 and HA and between HB and HC. Increased flexibility at low pH for residues 140–144 agrees with the reported pH sensitivity at the N-terminal end of HA (44). At middle pH, residues 136–139 showed higher flexibility. A marked increase in flexibility relative to neutral pH was observed for the HB-HC loop at middle and low pH. The different patterns of flexibility are related to conformational differences in this loop (Fig. 3 *C*).

Stability of secondary structure elements

In the majority of simulations, the three hydrogen bonds of the native β-sheet were populated for at least 90% of the time, but the population was decreased significantly for one or more hydrogen bonds in some simulations. In the fourth neutral-pH simulation, the hydrogen bond between Met^{129} N and Tyr^{163} O broke after 7.7 ns of simulation.

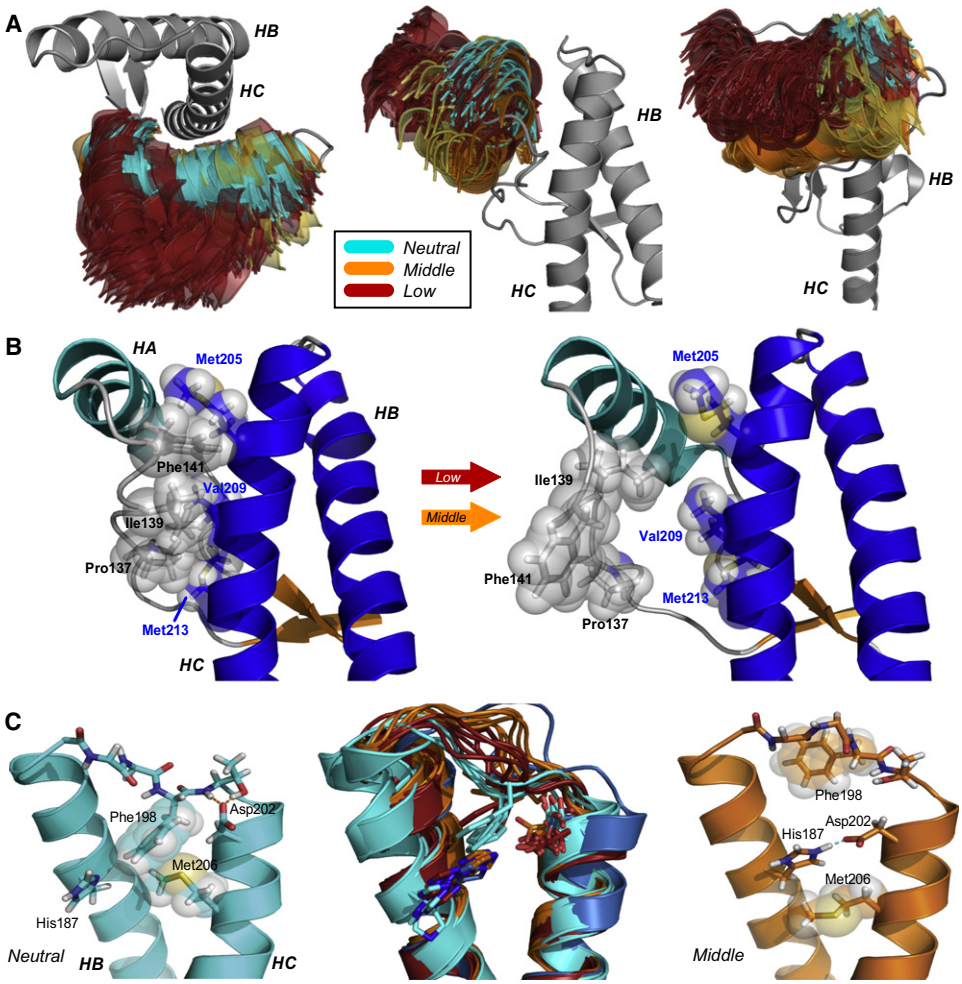

FIGURE 3 Main conformational changes observed in the middle- and low-pH simulations. (*A*) Helix A throughout the neutral- (*cyan*), middle- (*orange*, or *yellow* for simulation 5), and low- (*red*) pH simulations. HA conformations from all 15 simulations are depicted at 2 ns intervals. Three different views are shown, and for reference the starting structure is displayed in gray. (*B*) Example of the (lack of) hydrophobic packing of residues in the loop connecting S1 and HA to residues on HC. (*Left*) Starting structure. (*Right*) Snapshot at 10 ns from low-pH simulation 3. (*C*) Conformations of the HB-HC loop and related residues. (*Left*) Typical situation in the neutral-pH simulations, with Phe^{198} interacting with Met^{206}. (*Middle*) Snapshots of neutral- (*cyan*), middle- (*orange*), and low- (*red*) pH simulations after 40 ns of simulation. Simulation 1 at neutral pH, an outlier, is shown in blue. (*Right*) Typical situation after equilibration in the middle-pH simulations: His^{187} forms a salt bridge with Asp^{202}, preventing Phe^{198} from returning to the hydrophobic core. Please note that the colors refer to the online figures.

The same hydrogen bond showed low population throughout the fourth middle-pH simulation (42%) and during the last 14 ns of the third middle-pH simulation (59%). In the latter, the population of the Gly^{131}-Val^{161} hydrogen bond was also reduced (71% over the whole simulation). The decreased stability of the native sheet in a number of simulations may indicate that this is a weak spot in the PrP structure, as was recently suggested in experimental and theoretical studies (45,46). Changes in the native sheet conformation may also be related to the slow (micro- to millisecond) movement indicated by NMR relaxation measurements (8,43). Cysteine-scanning, site-directed spin labeling has shown that S2 is a pH-sensitive region (44).

None of the helices were lost in any of the simulations, but the final turn of HA (residues 153–156) was labile. In neutral-pH simulations, the turn formed a 3_{10} helix for 19–30% of the time, whereas only two middle-pH simulations showed significant periods of 3_{10} helix (9% and 7% of the time in simulations 3 and 5, respectively). The lack of structure at middle pH compared with neutral pH is consistent with the main conformational difference found by NMR: at pH 7, residues 153–156 formed a 3_{10} helix, whereas the conformation was less ordered at pH 4.5 (7,26). Calzolai and Zahn (26) suggested that this difference could be due to the repulsion of positive charges on His^{155} and Arg^{156} at lower pH, which is supported by our observation that the average distance between their side-chain nitrogens was 2.1 Å longer in the middle-pH simulations (from 10–50 ns). In the majority of the low-pH simulations and the fifth simulation at the middle-pH regime, the final turn of HA became fully α-helical. This change was not observed in any of the neutral-pH simulations and was related to displacement of HA, as discussed in the next section.

HB and HC were particularly stable around the disulfide bond (Cys^{179}-Cys^{214}). The population of $i \rightarrow i+4$ main-chain hydrogen bonds was generally >90% for residues 172–183 in HB and >85% for residues 200–224 in HC, in line with hydrogen/deuterium exchange protection factors (7,26). The population of hydrogen bonds in the C-terminal part of HB (residues 184–195) decreased with pH: 89%, 86% and 73% for neutral, middle, and low pH, respectively (outlier neutral-pH simulation 1 was not taken into account). This trend may be influenced by protonation of His^{187} (26), but protonation of Asp and Glu had a larger effect, for example, through restructuring of the HB-HC loop in response to protonation of Glu^{196}. No trend with pH was evident for hydrogen bonding in the C-terminal part of HC.

Increased movement of HA

Significant changes in the positioning of HA occurred in the middle- and low-pH simulations (Fig. 3 *A*, Fig. S4). Middle-pH simulations 3 and 4 featured a shift of the N-terminal end of HA downward. In low-pH simulations, the N-terminal end swung away from HC (Fig. 3 *A*, Fig. S4), especially in the second (after 4.7 ns), third (after 39.9 ns), and fifth (after 9.0 ns) simulations. A similar swing was observed in the fifth middle-pH simulation (after 20.7 ns). This repositioning was accompanied by a significant loss of contacts between HA and the rest of the globular domain, including a hydrogen bond between Tyr^{149} and Asp^{202} (Table S1).

In line with the conformational changes observed at middle and low pH, the tertiary contact region of HA was found to be highly pH-sensitive in mouse recPrP, with lowering of pH causing a marked increase in mobility (44). In previous simulations, our group (27–30), as well as Colacino et al. (47), observed an increase in mobility and positional changes of HA at low pH. Further, unfolding studies under high temperature, high pressure, or with denaturant indicated that HA and the preceding loop can rearrange and become detached from the remainder of the protein (48,49), and a partially misfolded conformation with a similarly displaced HA helix was found in replica exchange MD simulations (50). Together, these data suggest that increased mobility and repositioning of HA in response to a decrease in pH may be related to misfolding.

Instability in the hydrophobic core: changes in loop conformations

A core of interacting hydrophobic side chains can be defined in the prion protein (51) (Fig. 1 *A*). The interactions in this hydrophobic core may confer stability to the globular domain of PrP. By measuring the solvent accessibility of the side chains, we were able to assess the compactness of the hydrophobic core (Fig. 2 *C*). Whereas the SASA in neutral-pH simulations fluctuated around 350 $Å^2$ (with the first simulation again being an outlier), values were higher at middle pH, particularly for simulations 3 and 5, in which they varied between 380 and 840 $Å^2$. Three low-pH simulations (simulations 2, 3, and 5) displayed similar extreme behavior. The large changes in solvent accessibility must be related to conformational changes that expose hydrophobic surfaces. Such changes were detected experimentally between pH 4.4 and 6 (23), and can be further identified using our simulations.

The main cause of exposed hydrophobic surface in our simulations was a change in conformation of the loop between S1 and HA, particularly residues 137–141. In the starting structure and at neutral pH, Pro^{137}, Ile^{139}, and Phe^{141} interact with Met^{205}, Val^{209}, and Met^{213} on HC (Fig. 3 *B*). The importance of these interactions for stability is illustrated by the significant decrease in thermostability ($\Delta\Delta G$ ~3 kcal/mole) of M205A and M213A mutant PrP (52). The average number of hydrophobic atom-atom contacts between 137,139,141 and 205,209,213 at neutral pH was lower than in the starting structure (~25 vs. 45), illustrating the dynamic nature of the loop. In middle- and low-pH simulations with a large increase in solvent accessibility of the hydrophobic core (>600 $Å^2$), however, contacts

were dramatically reduced. Interestingly, the sensitivity to pressure of Ile^{139} and Phe^{141} in human PrP suggests local conformational freedom and indicates that this region may be a starting point for aggregation (53), as we proposed previously based on simulation and modeling (28,29,31,54). Our current simulations show that the loss of contacts and related exposure of hydrophobic surface precedes outward displacement of HA.

A further cause of increased exposure of hydrophobic surface area at middle and low pH is the positioning of Phe^{198}, which is located in the loop between HB and HC (residues 194–199). In the starting structure and in simulations at neutral pH, the Phe^{198} side chain was placed between the helices, where it formed many hydrophobic contacts, particularly with Met^{206}. At middle and low pH, the loop changed conformation and Phe^{198} swung out into solvent (Fig. 3 *C*). In two low-pH simulations, Phe^{198} partially returned to its original position, whereas this never happened at middle pH. Crystal structures of human PrP indicate that the HB-HC loop has increased conformational freedom: it forms the hinge in domain-swapped dimers (55,56) and it is part of the most disordered region in antibody-bound PrP (57). Further, binding of a PrP^{Sc}-specific antibody to an epitope in residues 187–206 (58) could be explained by a change in loop conformation exposing Phe^{198} during misfolding. The changes in the S1-HA and HB-HC connecting loops identified in the middle- and low-pH simulations expose Met residues (Met^{205} and Met^{213} are exposed by S1-HA loop movement, and Met^{206} is exposed by HB-HC loop movement). In vivo, exposure of these residues could lead to oxidation, which has been related to destabilization and conversion of PrP^{C} by MD simulation (59) and experiment (60).

Local pH-dependent changes around histidine residues

Significant pH-dependent changes in polar interactions are described in the Supporting Material. Here, we will focus on differences involving the four His residues in the globular domain (Fig. 1 *C*), as these may be involved in triggering pH-dependent misfolding. His^{140} is predicted to have the highest pK_a (61) and is therefore likely the first to be protonated when the pH decreases. At neutral and low pH, His^{140} was positioned predominantly out into solvent. At middle pH, a permanent salt bridge was formed with Asp^{147} (100% of the time in all simulations). This salt bridge was also found in previous MD simulations (61,62), but did not affect the Asp^{147}-Arg^{151} salt bridge that may stabilize HA (63). His^{155} and His^{177} were predominantly solvent-exposed at all pH regimes, in agreement with the structures obtained from NMR data measured at pH 7.0 (26) and 4.5 (7). In two middle-pH simulations, the His^{177} side chain formed a stable salt bridge (with Asp^{178} in simulation 3, and with Glu^{211} in simulation 4).

His^{187} is positioned between HB and HC and the C-terminal part of HA. Because of its buried location, it is likely to be the last His to become protonated as the pH decreases (61). At neutral pH, His^{187} donated a hydrogen bond to the backbone carbonyl of Arg^{156} for approximately one-third of the time, thereby linking HA and HB. This interaction is also found in the crystal structures of human recPrP (55,57) and in a fraction (20%) of the deposited NMR structures (7,26). However, it never formed in the middle- or low-pH simulations. Protonation of His^{187} may thus explain the triggering of instability and conformational change caused by lowering of pH. Of interest, mutation of His^{187} to Arg is linked to familial CJD (64). In all middle-pH simulations, His^{187} formed a stable salt bridge with Asp^{202} within 5 ns of simulation (Fig. 3 *C*). This interaction was made possible by the dislocation of Phe^{198}, and once the His^{187}-Asp^{202} salt bridge was formed, it prevented Phe^{198} from moving back to its original position.

Early misfolding at the middle-pH regime

The fifth simulation at middle pH showed significant conformational changes similar to those found previously in low-pH simulations and described as a potential conversion to a PrP^{Sc}-like conformation (29,30). Conversion and aggregation of recPrP was recently induced solely by lowering the pH to 4.0 and gentle rotation (24), and the simulation presented here provides insight into the detailed molecular mechanism of early misfolding that is required for aggregation at such conditions. The simulation is characterized by the addition of an extra strand onto the native β-sheet (Fig. 4), exposure of hydrophobic surfaces (Fig. 4), and significant movement of HA away from the HB-HC core (Figs. 3 *A* and 4 *A*).

The first event was the addition of an extra strand to the native β-sheet. From 1.65 ns, a β-bridge (two main-chain hydrogen bonds) formed between Ala^{120} and Leu^{130}. An additional hydrogen bond formed between the amide of Val^{122} and the carbonyl of Tyr^{128} during extended periods (from 6.2 ns), defining residues 120–122 as a β-strand interacting with S1. At certain periods (e.g., 33.2–36.3 ns), this strand extended to Gly^{123}. Between 40.5 and 42.6 ns, the beginnings of a second additional strand (residues 115–117) were observed (Fig. 4 *A*). Furthermore, significant protection to hydrogen exchange in the 117–133 region was recently observed in hamster PrP^{Sc} (65) and in fibrils formed from PrP 23–144 (66). In this particular simulation, further extension of the native sheet was blocked by the formation of a short α-helical segment (residues 106–114), which overlaps with the region that was indicated to have α-helical character based on theoretical predictions (67), simulation (68), and experiment (69). The formation of sheet-like conformations in previous simulations (27,30), as well as amyloid formation of peptides spanning this region (69–71), reflects the propensity of the N-terminal region of PrP to further extend the currently observed β-sheet.

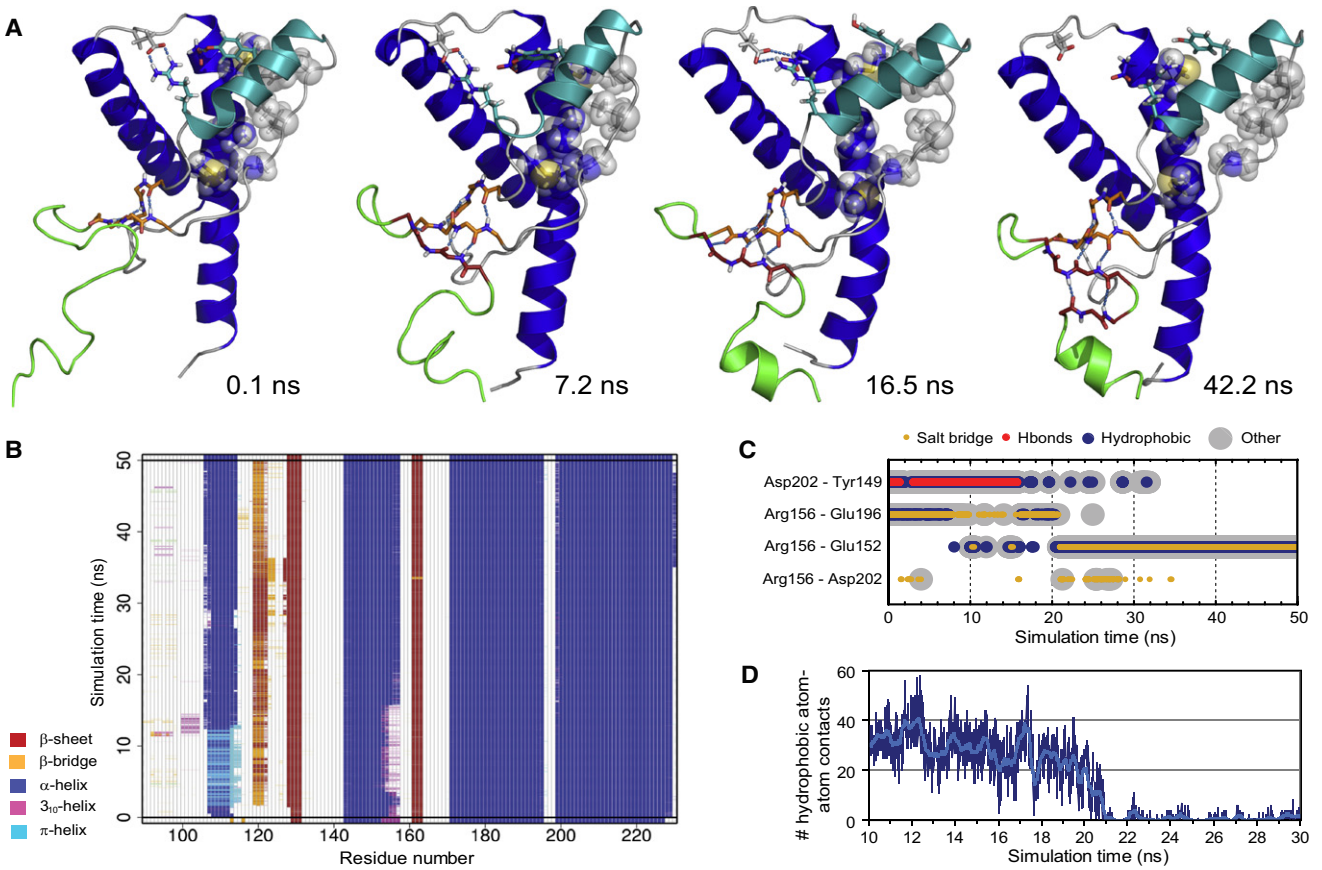

FIGURE 4 Early misfolding of PrP as observed at the middle-pH regime, simulation 5. (*A*) Snapshots from the trajectory at the indicated time points. The backbone is colored as in Fig. 1, with new strands in dark red (for online version). Relevant residues and hydrogen bonds are shown. For clarity, residues 90–105 are omitted. (*B*) Secondary structure analysis with all residues participating in hydrogen bonding marked as part of the secondary structure element. (*C*) Selected contacts over time. (*D*) Number of hydrophobic atom-atom contacts over time between residues 137,139,141 and 205,209,213. At 0 ns there are 45 contacts; at 50 ns none remain.

The misfolding trajectory showed significant exposure of hydrophobic residues (Fig. 2 *C*). An initial increase in the solvent accessibility of the hydrophobic core (~120 Å^2 within 1 ns) was due to the expulsion of Phe^{198} from the hydrophobic core. A second increase (by another ~230 Å^2) occurred between 15 and 23 ns and was related to the loss of hydrophobic contacts between the S1-HA loop and HC (Fig. 3 *B*). An initial decline to <10 hydrophobic atom-atom contacts occurred around 16 ns (Fig. 4 *D*). This decline started with Ile^{139} moving away from HC (losing all hydrophobic contacts from 15.6 ns) while Pro^{137} and Phe^{141} were still in contact. Thereafter, hydrophobic contacts further declined until no stable contacts remained.

In conjunction with the loss of hydrophobic contacts between the S1-HA loop and HC, HA moved away from the HB-HC core. After 15.75 ns, the hydrogen bond between Tyr^{149} and Asp^{202} broke (Fig. 4 *C*), and simultaneously residues 153–156 became α-helical. These events marked the first shift of the N-terminal end of HA away from HC. After 20.5 ns the Arg^{156}-Glu^{196} salt bridge broke, allowing for greater movement of HA that resulted in the N-terminal end moving further out into solvent. Shortly after the Arg^{156}-Glu^{196} salt bridge broke, Arg^{156} formed a stable salt bridge with Glu^{152} (Fig. 4 *C*). Arg^{156} occasionally formed a salt bridge with Asp^{202} also, an interaction that has also been observed in replica-exchange MD simulations (50).

Misfolding and aggregation

In this work we identified specific conformational changes and areas of instability related to a decrease in pH. These changes may be related to the misfolding and subsequent aggregation of PrP, which in turn results in neurotoxicity and formation of an infectious particle. Three main changes stand out: 1), extension of the native sheet into the flexible N-terminal domain; 2), movement of HA and the preceding loop out into solvent; and 3), rearrangement of the loop between HB and HC. The first two are related to regions involved in the binding interface between PrP^C and PrP^{Sc}: residues 98–110 and 136–140. Residues 136–140 were first predicted to form a strand based on MD simulations (28), and this region is important for oligomerization (29). New experimental data on amyloid formed from human PrP 23–144 (66) also support our proposal that these two regions

are brought together upon aggregation, as in the spiral protofibril models based on PrP conformations from MD simulations and in agreement with a range of experimental data (12,29,31,54). The misfolded conformation at middle pH identified here also fits into this general model, which may represent a toxic and soluble oligomeric state (72). In this conformation, the three helices are still largely intact, whereas refolding of HB and HC may be required for formation of the final amyloid fibril (24,73,74), although many experimental findings argue against that. Such restructuring would likely happen later in the aggregation process (75,76), and the pH-dependent changes in the HB-HC loop indicate that restructuring may start there, as proposed previously (55,77).

CONCLUSIONS

Extensive simulations of human PrP at three different pH regimes revealed detailed conformational and dynamical changes that can occur in low pH environments. The most significant change was the displacement of HA away from the HB-HC core. This movement was related to changes in the preceding loop that exposed a significant hydrophobic area. These changes, which can be directly related to experimental results, favor aggregation of PrP. Further changes involved extension of the native β-sheet and conformational changes in the loop connecting HB and HC. The detailed changes in conformation and dynamics of the prion protein in response to lowering of the pH described in this study are not only consistent with experimental data, they also provide insight into the mechanism of pH-induced misfolding. This information is being exploited for drug development, as aggregation of misfolded proteins is a crucial stage in the development of prion disease.

SUPPORTING MATERIAL

Six figures, one table, detailed methods, and further results are available at http://www.biophysj.org/biophysj/supplemental/S0006-3495(10)00937-9.

We thank Alex D. Scouras for technical assistance. Molecular images were created using PyMOL (78).

This study was supported by the National Institutes of Health (GM 81407). Computer resources were provided by the National Institutes of Health through the Multi-Tiered Proteomic Compute Cluster (NCRR 1S10RR023044-01).

REFERENCES

1. Aguzzi, A., and A. M. Calella. 2009. Prions: protein aggregation and infectious diseases. *Physiol. Rev.* 89:1105–1152.
2. Van der Kamp, M. W., and V. Daggett. 2009. The consequences of pathogenic mutations to the human prion protein. *Protein Eng. Des. Sel.* 22:461–468.
3. Cobb, N. J., and W. K. Surewicz. 2009. Prion diseases and their biochemical mechanisms. *Biochemistry.* 48:2574–2585.
4. Aguzzi, A., C. Sigurdson, and M. Heikenwaelder. 2008. Molecular mechanisms of prion pathogenesis. *Annu. Rev. Pathol.* 3:11–40.
5. Donne, D. G., J. H. Viles, …, H. J. Dyson. 1997. Structure of the recombinant full-length hamster prion protein PrP(29-231): the N terminus is highly flexible. *Proc. Natl. Acad. Sci. USA.* 94:13452–13457.
6. Riek, R., S. Hornemann, …, K. Wüthrich. 1997. NMR characterization of the full-length recombinant murine prion protein, mPrP(23-231). *FEBS Lett.* 413:282–288.
7. Zahn, R., A. Z. Liu, …, K. Wüthrich. 2000. NMR solution structure of the human prion protein. *Proc. Natl. Acad. Sci. USA.* 97:145–150.
8. Viles, J. H., D. Donne, …, P. E. Wright. 2001. Local structural plasticity of the prion protein. Analysis of NMR relaxation dynamics. *Biochemistry.* 40:2743–2753.
9. Caughey, B. W., A. Dong, …, W. S. Caughey. 1991. Secondary structure analysis of the scrapie-associated protein PrP 27-30 in water by infrared spectroscopy. *Biochemistry.* 30:7672–7680.
10. Pan, K. M., M. Baldwin, …, S. B. Prusiner. 1993. Conversion of α-helices into β-sheets features in the formation of the scrapie prion proteins. *Proc. Natl. Acad. Sci. USA.* 90:10962–10966.
11. Jackson, G. S., S. F. Hill, …, J. Collinge. 1999. Multiple folding pathways for heterologously expressed human prion protein. *Biochim. Biophys. Acta.* 1431:1–13.
12. Abalos, G. C., J. T. Cruite, …, L. Solforosi. 2008. Identifying key components of the PrP^{C}-PrP^{Sc} replicative interface. *J. Biol. Chem.* 283:34021–34028.
13. Brown, D. R., J. Herms, and H. A. Kretzschmar. 1994. Mouse cortical cells lacking cellular PrP survive in culture with a neurotoxic PrP fragment. *Neuroreport.* 5:2057–2060.
14. Forloni, G., N. Angeretti, …, F. Tagliavini. 1993. Neurotoxicity of a prion protein fragment. *Nature.* 362:543–546.
15. Supattapone, S., P. Bosque, …, M. Scott. 1999. Prion protein of 106 residues creates an artificial transmission barrier for prion replication in transgenic mice. *Cell.* 96:869–878.
16. Sunyach, C., A. Jen, …, R. Morris. 2003. The mechanism of internalization of glycosylphosphatidylinositol-anchored prion protein. *EMBO J.* 22:3591–3601.
17. Lee, R. J., S. Wang, and P. S. Low. 1996. Measurement of endosome pH following folate receptor-mediated endocytosis. *Biochim. Biophys. Acta.* 1312:237–242.
18. Arnold, J. E., C. Tipler, …, R. J. Mayer. 1995. The abnormal isoform of the prion protein accumulates in late-endosome-like organelles in scrapie-infected mouse brain. *J. Pathol.* 176:403–411.
19. Borchelt, D. R., A. Taraboulos, and S. B. Prusiner. 1992. Evidence for synthesis of scrapie prion proteins in the endocytic pathway. *J. Biol. Chem.* 267:16188–16199.
20. Caughey, B., G. J. Raymond, …, R. E. Race. 1991. N-terminal truncation of the scrapie-associated form of PrP by lysosomal protease(s): implications regarding the site of conversion of PrP to the protease-resistant state. *J. Virol.* 65:6597–6603.
21. Godsave, S. F., H. Wille, …, P. J. Peters. 2008. Cryo-immunogold electron microscopy for prions: toward identification of a conversion site. *J. Neurosci.* 28:12489–12499.
22. DeMarco, M. L., and V. Daggett. 2005. Local environmental effects on the structure of the prion protein. *C. R. Biol.* 328:847–862.
23. Swietnicki, W., R. Petersen, …, W. K. Surewicz. 1997. pH-dependent stability and conformation of the recombinant human prion protein PrP (90-231). *J. Biol. Chem.* 272:27517–27520.
24. Cobb, N. J., A. C. Apetri, and W. K. Surewicz. 2008. Prion protein amyloid formation under native-like conditions involves refolding of the C-terminal α-helical domain. *J. Biol. Chem.* 283:34704–34711.
25. Apetri, A. C., K. Maki, …, W. K. Surewicz. 2006. Early intermediate in human prion protein folding as evidenced by ultrarapid mixing experiments. *J. Am. Chem. Soc.* 128:11673–11678.
26. Calzolai, L., and R. Zahn. 2003. Influence of pH on NMR structure and stability of the human prion protein globular domain. *J. Biol. Chem.* 278:35592–35596.

27. Alonso, D. O. V., C. An, and V. Daggett. 2002. Simulations of biomolecules: characterization of the early steps in the pH-induced conformational conversion of the hamster, bovine and human forms of the prion protein. *Philos. Transact. A Math. Phys. Eng. Sci.* 360:1165–1178.
28. Alonso, D. O. V., S. J. DeArmond, …, V. Daggett. 2001. Mapping the early steps in the pH-induced conformational conversion of the prion protein. *Proc. Natl. Acad. Sci. USA.* 98:2985–2989.
29. DeMarco, M. L., and V. Daggett. 2004. From conversion to aggregation: protofibril formation of the prion protein. *Proc. Natl. Acad. Sci. USA.* 101:2293–2298.
30. DeMarco, M. L., and V. Daggett. 2007. Molecular mechanism for low pH triggered misfolding of the human prion protein. *Biochemistry.* 46:3045–3054.
31. Scouras, A. D., and V. Daggett. 2008. Species variation in PrP^{Sc} protofibril models. *J. Mater. Sci.* 43:3625–3637.
32. Beck, D. A. C., D. O. V. Alonso, and V. Daggett. 2000–2010. *In lucem* molecular mechanics. University of Washington, Seattle, WA.
33. Levitt, M., M. Hirshberg, …, V. Daggett. 1995. Potential-energy function and parameters for simulations of the molecular-dynamics of proteins and nucleic-acids in solution. *Comput. Phys. Commun.* 91:215–231.
34. Levitt, M., M. Hirshberg, …, V. Daggett. 1997. Calibration and testing of a water model for simulation of the molecular dynamics of proteins and nucleic acids in solution. *J. Phys. Chem. B.* 101:5051–5061.
35. Beck, D. A. C., and V. Daggett. 2004. Methods for molecular dynamics simulations of protein folding/unfolding in solution. *Methods.* 34: 112–120.
36. Lee, B., and F. M. Richards. 1971. The interpretation of protein structures: estimation of static accessibility. *J. Mol. Biol.* 55:379–400.
37. Kabsch, W., and C. Sander. 1983. Dictionary of protein secondary structure: pattern recognition of hydrogen-bonded and geometrical features. *Biopolymers.* 22:2577–2637.
38. Zhang, Y. B., W. Swietnicki, …, F. D. Sönnichsen. 2000. Solution structure of the E200K variant of human prion protein. Implications for the mechanism of pathogenesis in familial prion diseases. *J. Biol. Chem.* 275:33650–33654.
39. Reference deleted at proof.
40. Matsunaga, Y., D. Peretz, …, M. A. Baldwin. 2001. Cryptic epitopes in N-terminally truncated prion protein are exposed in the full-length molecule: dependence of conformation on pH. *Proteins.* 44:110–118.
41. Riek, R., S. Hornemann, …, K. Wüthrich. 1996. NMR structure of the mouse prion protein domain PrP(121-321). *Nature.* 382:180–182.
42. Calzolai, L., D. A. Lysek, …, K. Wüthrich. 2000. NMR structures of three single-residue variants of the human prion protein. *Proc. Natl. Acad. Sci. USA.* 97:8340–8345.
43. O'Sullivan, D. B. D., C. E. Jones, …, J. H. Viles. 2009. Dynamics of a truncated prion protein, PrP(113-231), from (15)N NMR relaxation: order parameters calculated and slow conformational fluctuations localized to a distinct region. *Protein Sci.* 18:410–423.
44. Watanabe, Y., O. Inanami, …, M. Kuwabara. 2006. Identification of pH-sensitive regions in the mouse prion by the cysteine-scanning spin-labeling ESR technique. *Biochem. Biophys. Res. Commun.* 350:549–556.
45. Blinov, N., M. Berjanskii, …, M. Stepanova. 2009. Structural domains and main-chain flexibility in prion proteins. *Biochemistry.* 48:1488–1497.
46. Julien, O., S. P. Graether, and B. D. Sykes. 2009. Monitoring prion protein stability by NMR. *J. Toxicol. Environ. Health A.* 72:1069–1074.
47. Colacino, S., G. Tiana, …, G. Colombo. 2006. The determinants of stability in the human prion protein: insights into folding and misfolding from the analysis of the change in the stabilization energy distribution in different conditions. *Proteins.* 62:698–707.
48. Hosszu, L. L. P., M. A. Wells, …, J. Collinge. 2005. Definable equilibrium states in the folding of human prion protein. *Biochemistry.* 44: 16649–16657.
49. Torrent, J., M. T. Alvarez-Martinez, …, R. Lange. 2005. The role of the 132-160 region in prion protein conformational transitions. *Protein Sci.* 14:956–967.
50. De Simone, A., A. Zagari, and P. Derreumaux. 2007. Structural and hydration properties of the partially unfolded states of the prion protein. *Biophys. J.* 93:1284–1292.
51. Riek, R., G. Wider, …, K. Wüthrich. 1998. Prion protein NMR structure and familial human spongiform encephalopathies. *Proc. Natl. Acad. Sci. USA.* 95:11667–11672.
52. Hart, T., L. L. P. Hosszu, …, A. R. Clarke. 2009. Folding kinetics of the human prion protein probed by temperature jump. *Proc. Natl. Acad. Sci. USA.* 106:5651–5656.
53. Kachel, N., W. Kremer, R. Zahn, and H. R. Kalbitzer. 2006. Observation of intermediate states of the human prion protein by high pressure NMR spectroscopy. *BMC Struct. Biol.* 6:16.
54. DeMarco, M. L., J. Silveira, …, V. Daggett. 2006. Structural properties of prion protein protofibrils and fibrils: an experimental assessment of atomic models. *Biochemistry.* 45:15573–15582.
55. Knaus, K. J., M. Morillas, …, V. C. Yee. 2001. Crystal structure of the human prion protein reveals a mechanism for oligomerization. *Nat. Struct. Biol.* 8:770–774.
56. Lee, S., L. Antony, …, V. C. Yee. 2010. Conformational diversity in prion protein variants influences intermolecular β-sheet formation. *EMBO J.* 29:251–262.
57. Antonyuk, S. V., C. R. Trevitt, …, J. Collinge. 2009. Crystal structure of human prion protein bound to a therapeutic antibody. *Proc. Natl. Acad. Sci. USA.* 106:2554–2558.
58. Jones, M., V. McLoughlin, …, M. W. Head. 2009. Production and characterization of a panel of monoclonal antibodies against native human cellular prion protein. *Hybridoma (Larchmt).* 28:13–20.
59. Colombo, G., M. Meli, …, M. Gasset. 2009. Methionine sulfoxides on prion protein helix-3 switch on the α-fold destabilization required for conversion. *PLoS ONE.* 4:e4296.
60. Wolschner, C., A. Giese, …, N. Budisa. 2009. Design of anti- and pro-aggregation variants to assess the effects of methionine oxidation in human prion protein. *Proc. Natl. Acad. Sci. USA.* 106:7756–7761.
61. Langella, E., R. Improta, …, V. Barone. 2006. Assessing the acid-base and conformational properties of histidine residues in human prion protein (125-228) by means of $pK_{(a)}$ calculations and molecular dynamics simulations. *Proteins.* 64:167–177.
62. Zuegg, J., and J. E. Gready. 1999. Molecular dynamics simulations of human prion protein: importance of correct treatment of electrostatic interactions. *Biochemistry.* 38:13862–13876.
63. Speare, J. O., T. S. Rush, 3rd, …, B. Caughey. 2003. The role of helix 1 aspartates and salt bridges in the stability and conversion of prion protein. *J. Biol. Chem.* 278:12522–12529.
64. Cervenáková, L., C. Buetefisch, …, L. G. Goldfarb. 1999. Novel PRNP sequence variant associated with familial encephalopathy. *Am. J. Med. Genet.* 88:653–656.
65. Smirnovas, V., J. I. Kim, …, W. K. Surewicz. 2009. Distinct structures of scrapie prion protein (PrP^{Sc})-seeded versus spontaneous recombinant prion protein fibrils revealed by hydrogen/deuterium exchange. *J. Biol. Chem.* 284:24233–24241.
66. Helmus, J. J., K. Surewicz, …, C. P. Jaroniec. 2008. Molecular conformation and dynamics of the Y145Stop variant of human prion protein in amyloid fibrils. *Proc. Natl. Acad. Sci. USA.* 105:6284–6289.
67. Huang, Z. W., J. M. Gabriel, …, F. E. Cohen. 1994. Proposed three-dimensional structure for the cellular prion protein. *Proc. Natl. Acad. Sci. USA.* 91:7139–7143.
68. Kazmirski, S. L., D. O. V. Alonso, …, V. Daggett. 1995. Theoretical studies of sequence effects on the conformational properties of a fragment of the prion protein: implications for scrapie formation. *Chem. Biol.* 2:305–315.
69. Zhang, H., K. Kaneko, …, S. B. Prusiner. 1995. Conformational transitions in peptides containing two putative α-helices of the prion protein. *J. Mol. Biol.* 250:514–526.
70. Gasset, M., M. A. Baldwin, …, S. B. Prusiner. 1992. Predicted α-helical regions of the prion protein when synthesized as peptides form amyloid. *Proc. Natl. Acad. Sci. USA.* 89:10940–10944.

71. Nguyen, J. T., H. Inouye, …, D. A. Kirschner. 1995. X-ray diffraction of scrapie prion rods and PrP peptides. *J. Mol. Biol.* 252:412–422.

72. Caughey, B., and P. T. Lansbury. 2003. Protofibrils, pores, fibrils, and neurodegeneration: separating the responsible protein aggregates from the innocent bystanders. *Annu. Rev. Neurosci.* 26:267–298.

73. Cobb, N. J., F. D. Sönnichsen, …, W. K. Surewicz. 2007. Molecular architecture of human prion protein amyloid: a parallel, in-register β-structure. *Proc. Natl. Acad. Sci. USA.* 104:18946–18951.

74. Lu, X. J., P. L. Wintrode, and W. K. Surewicz. 2007. β-Sheet core of human prion protein amyloid fibrils as determined by hydrogen/deuterium exchange. *Proc. Natl. Acad. Sci. USA.* 104:1510–1515.

75. Zou, W. Q., and N. R. Cashman. 2002. Acidic pH and detergents enhance in vitro conversion of human brain PrP^{C} to a PrP^{Sc}-like form. *J. Biol. Chem.* 277:43942–43947.

76. Bocharova, O. V., N. Makarava, …, I. V. Baskakov. 2006. Annealing prion protein amyloid fibrils at high temperature results in extension of a proteinase K-resistant core. *J. Biol. Chem.* 281:2373–2379.

77. Dima, R. I., and D. Thirumalai. 2004. Probing the instabilities in the dynamics of helical fragments from mouse PrP^{C}. *Proc. Natl. Acad. Sci. USA.* 101:15335–15340.

78. DeLano, W. L. 2002. The PyMOL Molecular Graphics System. DeLano Scientific, Palo Alto, CA.